

RESEARCH ARTICLE

Open Access



The middle atmospheric circulation of a tidally locked Earth-like planet and the role of the sea surface temperature

Elisavet Proedrou^{1,2*†} , Klemens Hocke^{1,2,3†} and Peter Wurz^{1,4}

Abstract

We investigate the influence of the sea surface temperature (SST) changes on the middle atmosphere of a tidally locked Earth-like planet orbiting a G star using the coupled 3D chemistry-climate model CESM1(WACCM). We perform three 90 day simulations. The first simulation is a present-day Earth (PDE) simulation, the second is a simulation of a tidally locked Earth-like planet with a tidally locked aquaplanet sea surface temperature (cold TLE (CLTE)) and the third is a hybrid simulation of a tidally locked Earth-like planet with a present-day Earth sea surface temperature (warm TLE (WTLE)). Our results show that changes in the SST have an influence on the lower stratospheric temperature and the secondary ozone layer. Both atmospheres exhibit a dayside upwelling and a nightside downwelling extending from the surface to the mesosphere. They are also characterised by comparable lower and middle stratospheric horizontal winds and relatively different mesospheric horizontal winds. The temperature of the WTLE atmosphere is altered as a result of the SST changes, compared to the CLTE. Specifically, the WTLE lower tropospheric temperature is increased by 3.7 K on average, due to the absorption of the increased upwelling longwave radiation and the increased sensible and latent heat. The WTLE upper troposphere temperature is decreased by 4 K on average, is adiabatic in nature, and is generated by the increased WTLE upwelling. The WTLE lower stratospheric temperature is increased by 3.8 K on average due to the absorption of the increased upwelling longwave radiation. The lower mesospheric temperature is decreased by 1.13 K on average due to increased mesospheric wave breaking. The upper mesospheric temperature is increased by 4.3 K, and its generation mechanism is currently unknown. Furthermore, the secondary ozone volume mixing ratio is increased by 40.5 %. The occurrence of large-scale vortices and variable jet streams depends, to some extent, on the SST distribution.

Keywords: Exoplanet, Tidally locked Earth, Middle atmosphere, Circulation, Atmospheric dynamics, Absorption lines, M star, Spectral line, SST, Sea surface temperature

Background

In this study, we simulate and analyse how differences in the underlying sea surface temperature (SST) of a tidally locked Earth-like planet orbiting a Sun-like star (TLE) alter its circulation and ozone distribution using a realistic, high-resolution, 3D chemistry-climate model.

To that end, we perform a pure TLE simulation, with the SST of the tidally locked aquaplanet generated by Merlis

and Schneider (2010) and a hybrid TLE simulation, which has the sea surface temperature of the present-day Earth. The hybrid simulation is not supposed to be a physical scenario and is only meant to test the importance of SST patterns for slowly rotating planets. We then compare the evolution of the ozone layer towards a steady state and determine their atmospheric structure and circulation. The study aims to determine the level of SST accuracy needed in simulations and observations of future of observed exoplanets.

The importance of the presence of an ozone layer in a planetary atmosphere is its ability to protect lifeforms from the harmful stellar UV radiation. It is, therefore, important for habitability studies, to determine whether

*Correspondence: elisavet.proedrou@iap.unibe.ch

†Equal contributors

¹Institute of Applied Physics, University of Bern, Sidlerstrasse 5, 3012 Bern, Switzerland

²Center for Space and Habitability, University of Bern, Sidlerstrasse 5, 3012 Bern, Switzerland

Full list of author information is available at the end of the article

very different underlying SSTs will significantly alter a planet's ozone layer.

Currently, planets located in the habitable zones of M stars are considered prime targets for the search for terrestrial habitable exoplanets (Tarter et al. 2007). This is due to the abundance of M stars and a good mass and radius star-to-planet ratio. Furthermore, the detection of planets orbiting an M star is easier due to the close proximity of the habitable zone to the M star and leads to a higher probability of the planet becoming tidally locked.

Haberle et al. (1996), Joshi et al. (1997) and Joshi (2003) showed that terrestrial planets located in an M star's habitable zone (0.02–0.2 AU) (Tarter et al. 2007) would be habitable provided that liquid water and the chemical constituents necessary for the emergence of life existed for a sufficiently long period of time. The flaring activity of M stars has been cited as a danger for the habitability of such planets; however, Segura et al. (2010) showed that the flares should not present a threat for the surface life. In our study, we investigate the ozone distribution and, therefore, one condition for the habitability of a tidally locked exoplanet revolving around an M star.

Due to being less massive than the Sun, M stars have weaker UV and visible emission and their spectrum peaks in the infrared. However, the enhanced stellar activity of M stars can result in the generation of flares whose EUV and UV emission is stronger than those of the quiet Sun. The different stellar spectral energy distributions will impact the planet's ozone distribution and the atmospheric temperature structure. Selsis et al. (2000), Segura et al. (2003), Segura et al. (2005), Grenfell et al. (2007), Rugheimer et al. (2013), Rauer et al. (2011) and Godolt et al. (2015) investigated the impact of different stellar spectral energy distributions on the ozone distribution of habitable non-tidally locked terrestrial extrasolar planets.

Selsis (2000) simulated the evolution of the chemical and thermal atmospheric structure of an Earth-like planet's when placed in the orbit of a F9 and K2 star using a 1D atmospheric model. He reported that an increase in the UV/visible light ratio results in the thickening of the planetary ozone layer compared to the Earth.

Segura et al. (2003) calculated the spectra of Earth-like planets orbiting a F2V, a G2V and a K2V star using a 1D coupled radiative-convective photochemical model and determined that the F2V planet would have a lower ozone concentration compared to the G2V or a K2V planet. This contrasts with the results of Selsis et al. (2000).

Segura et al. (2005) calculated the spectra of Earth-like planets orbiting a M star and determined that an ozone layer similar to that of the Earth would develop.

Grenfell et al. (2007) calculated the atmospheric composition changes of an Earth-like planet when subjected to 5–10 % changes of its orbital position around a G2V,

a F2V, and a K2V star using a 1D coupled radiative-convective photochemical column model. As the planet moved outwards, the ozone increased by ~10 % due to the decreased stratospheric temperature.

Rugheimer et al. (2013) used a geometrical 1D model global atmosphere model to simulate the spectra of clear and cloudy Earth-like planets orbiting a F, a G, and a K star at the 1 AU equivalent distance. They reported that an increase in either the parent star's UV radiation or its temperature resulted in increased O₃ concentrations and stronger O₃ spectral features.

Rauer et al. (2011) used a plane-parallel, 1D climate model, coupled with a chemistry model to calculate the molecular absorption bands of super-Earth planetary atmospheres orbiting M stars. They reported that the ozone emission of planets orbiting quiet warm M0–M3 dwarfs would be stronger than the Earth's. The ozone emission spectra of planets orbiting cool and quiet M4–M7, on the other hand, stars would be weaker due to increases in the planet's mid-atmospheric temperatures.

Grenfell et al. (2013) used a global-mean radiative-convective-photochemical column model to perform a sensitivity study on the atmosphere of an Earth-like planet. The stellar class and planetary gravity of the planet was varied and the effects of the resulting photochemistry and climate changes investigated. According to their results, the stratospheric ozone generation of an Earth-like planet orbiting an M0 star is still dominated by the Chapman cycle but to a lesser extent compared to the Earth and the smog generation mechanism is strengthened. The Chapman cycle is a set of chemical and photochemical reactions responsible for the formation and destruction of ozone that involves only oxygen reactions. Moving towards cooler stars, the Chapman mechanism is weakened and the smog mechanisms is strengthened. For cool M5–M7 stars, the ozone photochemistry shifted completely from the Chapman production to smog-dominated stratospheric ozone production.

Godolt et al. (2015) studied the influence of F, G and K stars on the stratospheric temperature, climate and potential habitability of Earth-like exoplanets using a state-of-the-art 3D Earth climate model which accounted for local and dynamical processes. They used a fixed Earth-like atmosphere with no atmospheric chemistry and positioned the planets at orbital distances that ensured that the total amount of energy received from the parent stars would equal the solar constant. The results of the study confirmed that when the atmospheric chemistry is maintained unaltered, different stellar spectral energy distributions will result in different ozone heating rates and, therefore, different vertical temperature structures, in accordance with Selsis (2000), Segura et al. (2003), Segura et al. (2005), Grenfell et al. (2007), Rugheimer et al. (2013) and Rauer et al. (2011). Specifically, the stratospheres of

Earth-like planets orbiting stars less massive than the Sun will be characterised by lower ozone heating rates and shallower stratospheric temperature increases compared to the Earth.

The above studies demonstrated that for non-tidally locked, M star orbiting planets, the reduced UV radiation emission would result in a cooler stratosphere and changes in their stratospheric ozone concentration. It is reasonable to assume that tidally locked planets would be equally affected.

The ozone concentration of a tidally locked Earth-like planet orbiting an M star would be altered by the effects of the tidal lock and the altered stellar irradiance spectrum and make the attribution of the ozone distribution changes on either the tidal lock or the altered UV radiation exceedingly challenging. Therefore, we chose to not include the effects of the altered UV radiation in our study and focus only on the impact of the tidal locking on the Earth-like planet orbiting a Sun-like star.

Past studies of tidally locked Earth-like atmospheres limited themselves to the troposphere (Merlis and Schneider 2010; Yang et al. 2013; Grenfell et al. 2014).

Merlis and Schneider (2010) simulated the troposphere of an Earth-like, tidally locked aquaplanet with a rotation period equal to one Earth year using an ideal gas GCM with an active hydrological cycle, a grey radiation scheme and a slab ocean. They reported a maximum subsolar point surface temperature of ~ 300 K and a minimum antisolar point temperature of 240 K. Since the surface temperature never dropped below 240 K, no atmospheric collapse occurred on the nightside. They also reported the presence of a strong upwelling above the subsolar point on the dayside and a downwelling, centred over the antisolar point, on the nightside. The upwelling was generated by the increased radiative heating, while the downwelling was generated by the increased radiative cooling.

Yang et al. (2013) demonstrated that clouds in the troposphere of a tidally locked aquaplanet, especially when located over the subsolar point, can ensure habitability at almost twice the Earth stellar flux.

Grenfell et al. (2014) used a global-mean, stationary, hydrostatic, atmospheric column model, extending from the surface to ~ 70 km, to perform a 1D simulation of an Earth-like exoplanet atmosphere. The planet's atmosphere had the starting composition, pressure and temperature of the 1976 Wikipedia US Standard Atmosphere (2016). The UV emission of a cool M7 star was varied, and the resulting climate-photochemical response of the planetary atmosphere, including numerous catalytic processes of O_3 depletion, were calculated. Grenfell et al. (2014) showed that the strongest O_3 emission was generated when the stellar UV radiative flux is ten times that of an M7 star. They also reported that the exoplanet's O_3

$9.6 \mu\text{m}$ spectral line profile was influenced strongly by the 200–350 nm UV output of the parent star.

The influence of the sea surface temperature on the tropospheric and lower stratospheric temperature and dynamics has been investigated by several researchers for the present-day Earth but not for exoplanets.

Braesicke and Pyle (2004) investigated the dynamics and ozone sensitivity to different SSTs using the Met Office Unified Model with simple stratospheric chemistry. They performed multi-annual simulations, each lasting 20 years. The simulations shared the same simplified ozone chemistry but different prescribed SSTs. According to their results, the appearance of extreme events in the winter stratosphere were more strongly correlated with the underlying SSTs rather than with changes of the ozone layer.

Rosenlof and Reid (2008) used data provided by the NOAA/CIRES Climate Diagnostics Center to investigate the long-term tropical lower stratospheric temperature trends over the western Tropical Pacific Ocean, in relation to variations in the SST. Their study revealed the presence of an anticorrelation between stratospheric temperature anomalies and SST anomalies. Rosenlof and Reid (2008) proposed the existence of a fairly direct influence between the underlying ocean and the lower tropical stratosphere and speculated that the anticorrelation is generated by the increased deep tropospheric convection generated by the SST warming.

Decker and Dameris (2008) reported the presence of a lower stratospheric cooling due to higher tropical SSTs. Their study investigated how the strength of the tropical upwelling is influenced by changes in the underlying SST and greenhouse gas concentrations. To that end, they performed two simulations with different SSTs and greenhouse gas concentrations. They concluded that the deep convection was amplified by the higher underlying SST and waves were generated. The waves enhanced the residual meridional circulation and the upwelling of ozone-poor tropospheric air into the lower stratosphere in the tropics.

One study by Hegy et al. (2014) was performed using the Community Earth System Model 1 (Whole Atmosphere Community Climate Model) (CESM1(WACCM)) version 1.0.2 to investigate the initial transient response of the boreal winter stratospheric polar vortex to localised SST warming events. They conducted 20 perpetual winter simulations. According to their results, the polar vortex was weakened by changes in the eddy-driven mean meridional circulation and negative anomalies appeared in the eddy momentum flux convergence. They also demonstrated that the initial state and subsequent internal variation of the extratropical atmosphere is equally important to the type of SST forcing in determining the response of the stratospheric polar vortex. Furthermore,

they found that the interactions between the internal variability of the vortex and the SST-driven wave anomalies govern the nature of the polar vortex response to the forcing.

Chen et al. (2010) used an Earth-like aquaplanet general circulation model to study the tropospheric winds and stratospheric Brewer-Dobson circulation sensitivities to SST warmings. The main aim of the study was to investigate the relationship between a warming ocean due to global warming and a change in the Earth's large-scale atmospheric circulation. The authors concluded that the location and sign of the SST perturbations gradient strongly influenced the tropospheric jet and the Hadley cell. They reported an increase in the Brewer-Dobson circulation in the presence of a low-latitude warming and a decrease in the presence of a high-latitude warming extending to the subtropics.

To the extent of our knowledge, the correlation between the SST and the middle atmosphere has not been investigated for a tidally locked Earth-like planet whose circulation largely differs from the Brewer-Dobson circulation of the fast rotating, present-day Earth.

Furthermore, the majority of the exoplanet and tidally locked exoplanet studies to date were performed using 1D and 2D models, and atmospheric transport processes are generally not accurately represented in such models. The few studies performed using a 3D model either focused entirely on the exoplanet's troposphere (Yang et al. 2013; Merlis and Schneider 2010) or studied the stratospheric dynamics, without taking into consideration the stratospheric chemistry and photochemistry (Godolt et al. 2015). None of the past studies investigated the exoplanets' mesosphere. They also did not study how the secondary ozone layer found in the Earth's mesosphere would be affected by the changes in parent star's stellar class, its distance from the star or the planet's tidal locking.

In a tidally locked Earth-like planet, the majority of the stratospheric ozone is located in the lower stratosphere and its distribution depends strongly on the atmospheric transport processes, as shown in Proedrou and Hocke (2016). Our current study uses a 3D realistic chemistry-climate global circulation model, extending from the surface to the top of the mesosphere. The 3D nature of the model and its inclusion of dynamics, chemistry and photochemistry will allow us to correctly calculate the exoplanet's ozone distribution and how a change in the underlying SST will affect it.

The sensitivity of the mesospheric conditions to SST variations is crucial for the observations of the spectral signatures of mesospheric gases, who will be affected by altered temperatures and/or circulation patterns.

Below, we first describe the model used and the simulation setup. Next, we present and analyse the atmospheric evolution to a steady state, the atmospheric circulation,

the atmospheric temperature structure and the ozone volume mixing ratio distribution (O_3 VMR).

Model description

The simulation is performed using the CESM version 1.04 which consists of five fully coupled geophysical models: atmosphere (ATM), land (LND), ocean (OCN), sea-ice (ICE) and land-ice (GLC). The models have five possible different modes: fully prognostic, data, stub and dead. The fully prognostic mode provides "state-of-the-art climate prediction and analysis tools" (Vertenstein et al. 2012).

The atmospheric model used to perform our study is the Whole Atmosphere Community Climate Model version 4 (CESM1(WACCM)) (Neal et al. 2012). CESM1(WACCM) has been used to simulate the circulation, gravity waves and atmospheric composition changes of the present-day Earth by Pedatella et al. (2014), Pedatella and Liu (2013), Lu et al. (2012), Tan et al. (2012a, 2012b, 2012c), Davis et al. (2013) and Smith et al. (2012). It is fully coupled to the land, ocean and ice models (Vertenstein et al. 2012).

It has a fully compressible horizontal discretisation and a quasi-Lagrangian vertical discretisation approximation which is good for scales larger than 10 km (Neal et al. 2012). It has 66 vertical levels starting on the surface of the planet and up to 5×10^{-6} hPa (2.5–149 km). The model top is located at ~ 150 km. The vertical coordinate is terrain following below 100 hPa and purely isobaric above 100 hPa. The vertical resolution is 1.1 km in the troposphere, 1.1–1.4 km in the lower stratosphere, 1.75 km at the stratopause and 3.5 km above 65 km (Neal et al. 2012).

CESM1(WACCM) has full tropospheric, stratospheric and mesospheric chemistry, with 57 chemical species (Neal et al. 2012). The gas-phase chemistry is coupled to the Modal Aerosol Model (Neal et al. 2012). The stratospheric distributions of long-lived species are taken from previously performed CESM1(WACCM) simulations.

The longwave and shortwave radiative transfer calculations are provided by the radiation code RRTMG (Iacono et al. 2008; Mlawer et al. 1997). It is capable of efficiently calculating the irradiance and heating rate in broad spectral intervals, while retaining a high level of accuracy relative to measurements and high-resolution line-by-line models. It also distinguishes between the direct and scattered solar radiation.

The shortwave radiative transfer is calculated over 14 bands (0.2 to 12.2 μm) while the longwave radiative transfer is calculated over 16 bands (3.1 to 1000.0 μm). The 16th longwave band includes the infrared contribution from the spectral interval below 3.1 μm . Above 65 km, the model covers the spectrum interval between soft X-rays and extreme ultraviolet irradiances (0.05 nm to Lyman- α (121.6 nm) and the spectrum interval between the Lyman- α (121.6 nm) and 100 μm (Neale et al. 2012).

The total shortwave fluxes are accurate within 1–2 W/m² compared to the standard RRTM SW for clear sky conditions and aerosols and 6 W/m² in overcast sky conditions. The total longwave fluxes are accurate within 1.0 W/m² at all levels. “The longwave radiative transfer is performed over a single angle for one upward and one downward calculation” (Neale et al. 2012). The absorption coefficients for the *k*-distributions for both the shortwave and the longwave radiation calculations in RRTMG are obtained from the line-by-line radiation model LBLRTM (Clough and Iacono 1995; Clough et al. 2005).

The calculation of the photolysis coefficients is divided into the 120–200 nm and 200–750 nm regions. The total photolytic rate constants are calculated by the model by integrating the product of the wavelength-dependent exo-atmospheric flux, the atmospheric transmission function, the molecular absorption cross section and the quantum yield for each absorbing species. The exo-atmospheric flux is taken from observations and varies over the 11 year solar sunspot cycle. The transmission function is wavelength-dependent and a function of the model abundance of ozone and molecular oxygen. For wavelengths above 200 nm, the molecular absorption cross section and the quantum yield are calculated by the model, while below 200 nm, their values are pre-defined. For NO and O₂ detailed photolysis and parametrisations are included in the model. The impact of clouds on the photolysis rates is parametrised. The impact of tropospheric and stratospheric aerosols on photolysis rates, on the other hand, is not calculated (Neale et al. 2012).

The CESM model uses the Kurucz solar source function, whose radiative transfer calculation is based upon solar measurements. The model assumes a total solar irradiance at the top of the atmosphere equal to TSI = 1368.22 W/m². The value is then “scaled in each spectral band through the specification of a time-varying solar spectral irradiance” (Neale et al. 2012). A combination of solar parametrizations is used to specify spectral irradiances over the soft X-ray to Lyman- α and the Lyman- α to 100 μ m spectral interval. The first spectral interval fluxes are calculated using the parametrization of Solomon and Qiang (2005). It accepts as input the 10.7 cm solar radio flux (*f* 10.7), whose daily values are obtained from the NOAA’s Space Environment Center (www.sec.noaa.gov) and its 81 day average. The second spectral interval fluxes are calculated using the empirical model of the wavelength-depending sunspot and facular influences (Lean et al. 2000; Wang et al. 2005; Neal et al. 2012).

The modelled sources of radiation absorption and scattering in the shortwave electromagnetic spectrum are H₂O, O₃, CO₂, O₂, CH₄, N₂, clouds, aerosols and Rayleigh scattering. The sources of molecular radiation absorption

in the longwave electromagnetic spectrum are H₂O, CO₂, O₃, N₂O, CH₄, O₂, N₂, CFC-11 and CFC-12. The shortwave electromagnetic radiation is calculated only for zenith angles larger than zero (Neale et al. 2012). The zonal mean climatology of the local O₃ concentration, the temperature, the overhead column O₃ and other chemicals is based on satellite and in situ Earth observations (Neal et al. 2012).

The model computes the chemical equilibrium of 36 photochemical species (O₂, O₃, N₂O, NO, NO₂, N₂O₅, HNO₃, NO₃, HO₂NO₂, CH₃OOH, CH₂O, H₂O, H₂O₂, Cl₂, ClO, OCIO, Cl₂O₂, HOCl, HCl, ClONO₂, BrCl, BrO, HOBr, BrONO₂, CH₃Cl, CCl₄, CH₃CCl₃, CFC11, CFC12, CFC113, HCFC22, CH₃Br, CF₃Br, CF₂ClBr, CO₂, CH₄). The model atmospheric tracers are O_x, NO_x, HO_x, ClO_x and BrO_x chemical families, excluding O₂, along with CH₄ and its degradation products. The main photochemical and chemical interactions responsible for changing the atmospheric ozone concentration are described by the reaction rate of ozone $\frac{d(O_3)}{dt} + J_{O_3}(O_3) + k_3(O)(O_3) + a_2(H)(O_3) + a_6(OH)(O_3) + a_{6b}(HO_2)(O_3) + b_4(NO)(O_3) + b_9(NO_2)(O_3) + d_2(Cl)(O_3) + e_2(Br)(O_3) = k_2(M)(O_2)(O)$. Where $\frac{d(O_3)}{dt}$ is the production rate of O₃, J_{O_3} is the photolysis rate of the ozone and $k_3, a_2, a_6, a_{6b}, b_4, b_9, d_2, e_2, k_2(M)$ are the chemical rate constants of the reactions and are taken from JPL06-2 (Sander et al. 2006).

A polar stratospheric cloud parametrisation scheme is incorporated in the model. It is activated when the cosine of the solar zenith angle is larger than zero at stratospheric altitudes and the stratospheric temperature drops below 195 K (Neal et al. 2012).

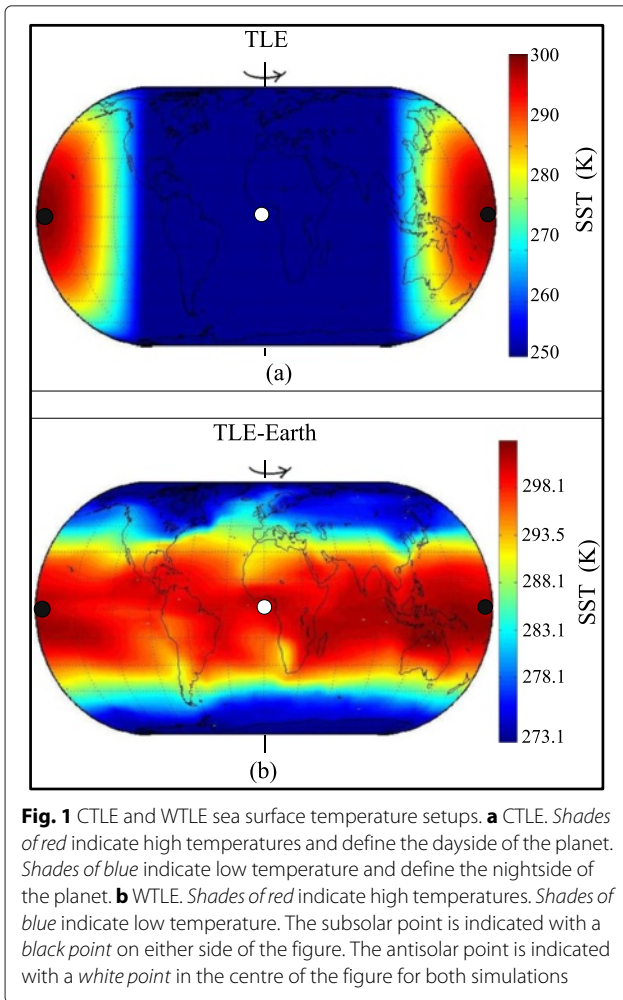
The momentum, sensible heat flux, latent heat flux, land surface albedos and upward longwave electromagnetic radiation are used to calculate the atmospheric radiation. The upward longwave radiation is given by the difference of the incident and the absorbed fluxes. The incident flux values are, in turn, determined from the daily values of the solar radio flux (*F* 10.7) which are provided by the National Oceanic and Atmospheric Administration’s (NOAA) Space Environment Center (2016).

The starting values of the zonal mean climatology of the local O₃ concentration, the temperature, the overhead column O₃ and other chemicals used by the model are provided by satellite and in situ Earth observations (Neal et al. 2012). A detailed model description can be found in Neal et al. (2012).

Methods

Simulation setup

We perform three 90 day simulations. Two for a TLE planet, with different SST distributions, and one for the present-day Earth (Fig. 1).



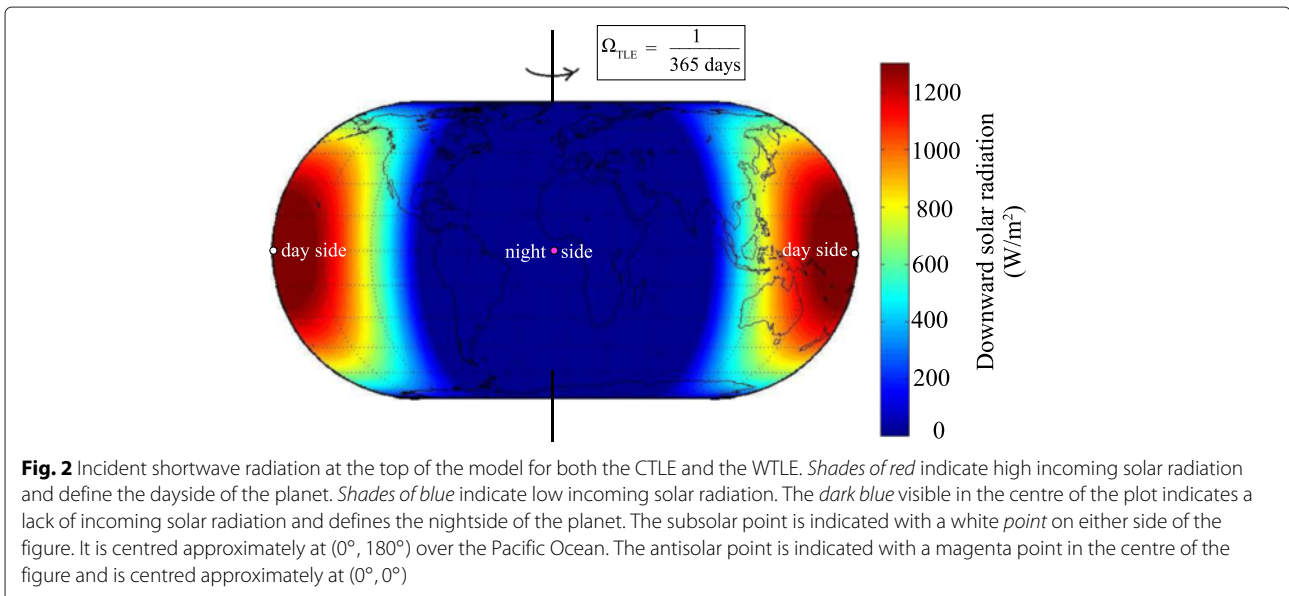
The present-day Earth simulation is an unaltered simulation of the present-day Earth, which starts on the Spring Equinox (21.03.2000) and ends 90 days later (18.06.2000).

The TLE simulations simulate a tidally locked Earth-like planet orbiting a Sun-like star. The tidally locked planets are located at a distance of 1 AU from the parent star and have the same eccentricity as the present day Earth, a stellar irradiance at the top of the model $1366.96 < S_0 < 1368.60$ and a rotation rate that is 1/365th of the Earth's rotation rate. Both of their subsolar points are permanently located (0.17° N, -178.17° E), which is the position of the Earth's subsolar point at 00:00 UT on the day of the Spring Equinox (21.03.2000).

The parameters altered to achieve the tidal lock and a perpetual equinox are:

- The number of seconds in a sidereal day: altered from 86,164 s/day to 3.15×10^7 s/day
- The planet's rotational velocity: set to 2.31×10^{-12} rad/s
- The planet's new rotation rate: set to 1° every 87,600 s (the Earth's rotation rate is 1° every 240 s)
- The position of the subsolar point: set to (0.17° N, -178.17° E) for the duration of the simulations
- The SST: changed to resemble the SST reported by Merlis and Schneider (2010)
- The solar zenith angle (SZA): set to a constant value by means of the present-day Earth (PDE) Julian date.

The SZA is the main parameter used for the assessment of the incoming solar radiation in the CESM model. By setting the Julian date to a constant value we stop the periodic 24 h variation of the SZA at all grid points. Figure 2 shows the shortwave solar radiation flux at the top of the model for the WTLE and CTLE simulations. The solar



point is depicted by a white dot located on either side of the figure, while the antisolar point is depicted by a magenta point located in the centre of the figure.

As mentioned in the Introduction, the tidally locked planets are identical except for their sea surface temperature distributions. The pure TLE SST distribution resembles the SST reported by Merlis and Schneider (2010) (Fig. 1b). It was characterised by a uniform nightside SST of 250 K and a monotonically and isotropically increasing dayside SST that reached a maximum of 300 K within a 30 degrees radius centred on the subsolar point. On account of the overall cooler SST, the simulation will be called cold TLE (CTLE).

The hybrid TLE SST distribution is that of the present-day Earth. It is characterised by temperatures of 290–300 K in the tropics and 270–280 K in the polar regions. Due to the overall warm SST, the simulation using this SST will be hereafter called warm TLE (WTLE). This WTLE simulation is not a realistic physical scenario but is rather used to test the importance of SST patterns for slowly rotating planets. Both SSTs can be seen in Fig. 1.

The CESM1(WACCM) requires the presence of an active land model and, therefore, has the general topography and continents of the Earth. The atmospheric and surface initialisation data are identical for all simulations and all start with same 3D ozone and wind fields.

In the next subsection, we present the middle atmospheric circulation (Ω , HW) and temperature (T) and ozone distribution (TOC, O_3 VMR) of the two simulations and we discuss the degree by which they are influenced by the two extreme SSTs. We first discuss the atmospheric adjustment time of the two tidally locked Earths (TLEs) and compare it to the present-day Earth. Then, we present and discuss their atmospheric circulation, atmospheric temperature structure and latitude-longitude O_3 VMR cross section.

It should be noted that while the possibility of tidal locking of an Earth-like planet within the habitable zone of a Sun-like star has a low probability, the similarity of the solar spectrum and atmospheric composition to the PDE fosters the intercomparison and interpretation of the differences in the model runs. Furthermore, since several past studies of tidally locked exoplanets have used models with solar spectrum and atmospheric composition similar to that of the PDE, this setup fosters the intercomparison and interpretation of the changes with past models."

Data analysis

The zonal wind (U), the meridional wind (V), the vertical wind (Ω), the atmospheric temperature (T), the air number density (M) and the O_3 VMR are extracted from the output datasets of the simulation run. The above parameters are then interpolated for the altitudes of 1 to 140 km. Next, the zonally averaged zonal, meridional and vertical

wind are calculated from 5 to 110 km. The O_3 concentration is calculated for the altitudes of 1 to 110 km by multiplying the ozone volume mixing ratio with the air number density ($[O_3] = O_{3VMR} \times [air]$). As a next step, the total ozone column density (TOC) is calculated by interpolating the O_3 concentration between the altitudes of 5 and 110 km ($TOC = \int_5^{110} [O_3] dz$). The altitude limits are imposed in order to avoid the data gaps generated by the presence of several high mountains and mountain ranges at low altitudes (e.g Himalayas, Kilimanjaro) and the air density data gaps above 110 km altitude. The TOC, HW, Ω and T global means are determined by calculating their zonal means as a function of latitude and then weighting them with the surface area of the latitude belts (surface area preserving mean). The change in percent between the CTLE and WTLE parameters is calculated using the following equation:

$$\Delta = \frac{\text{parameter}_{CTLE} - \text{parameter}_{WTLE}}{\text{parameter}_{WTLE}} * 100 \quad (1)$$

where the term parameter is used to refer to any of the TOC, Ω , HW, T and O_3 VMR.

Terminology

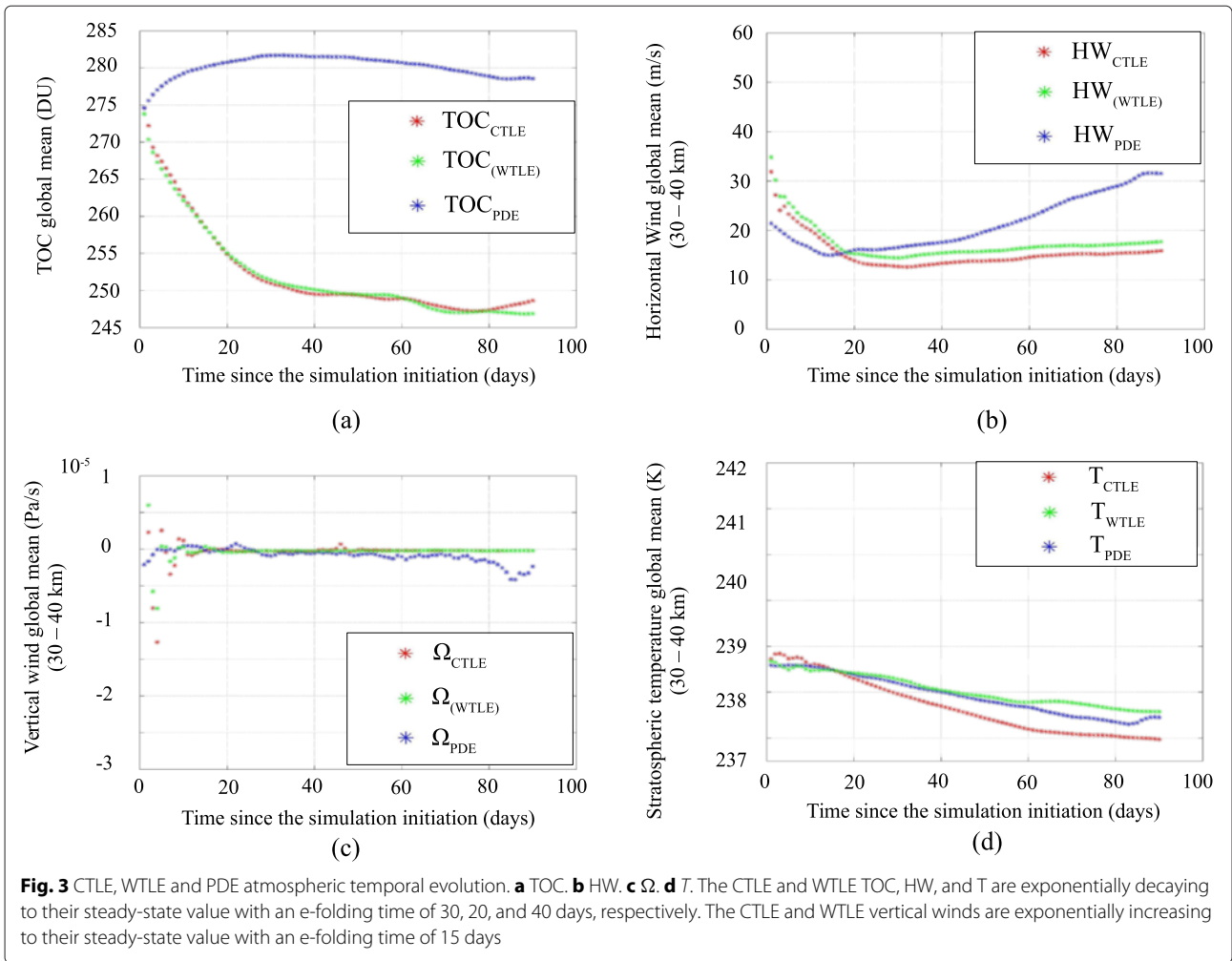
The dayside of a tidally locked planet is the permanently illuminated hemisphere that is always facing the parent star, while the nightside is the hemisphere that is never illuminated by the parent star. The subsolar point is defined as the position of maximum solar flux, located at the centre of the dayside and has a SZA equal to zero ($SZA = 0^\circ$). The antisolar point is defined as the centre of the nightside ($SZA = 180^\circ$).

Results and discussion

Atmospheric steady state

According to our results, the middle atmospheres of the CTLE and WTLE adjust to the new radiative and dynamical conditions, reaching a steady-state condition within 80 days from the start of the simulation. Figure 3 shows the adjustment times of the CTLE and WTLE total ozone column (TOC), and the global-mean stratospheric horizontal wind (HW), global-mean stratospheric vertical wind (Ω) and global-mean stratospheric temperature (T) for the 30–40 km altitude range. The temporal evolutions of the PDE TOC, HW, Ω and T are also provided.

The CTLE and the WTLE TOC, HW and Ω adjustment times and values are not significantly altered by the SST change, as can be seen in Fig. 3a–c. The percent change in their adjustment times is shown in Table 1. The CTLE and WTLE T adjustment times are shown in Fig. 3d. As one can see, their adjustment times are comparable despite their altered slope and the CTLE values are decreased compared to the WTLE. This difference is also visible



in the CTLE and WTLE T global average which will be presented in the “Vertical wind” section.

The CTLE and WTLE e-folding times of the TOC, HW, Ω and T along with their PDE equivalents and standard deviations (σ) are shown in Table 1. They are 30, 20, 15 and 40 days, respectively. Therefore, their adjustment times are 60, 40, 30 and 80 days, respectively. A comparison between the CTLE, the WTLE and the PDE σ in Table 1 reveals that the PDE has higher standard

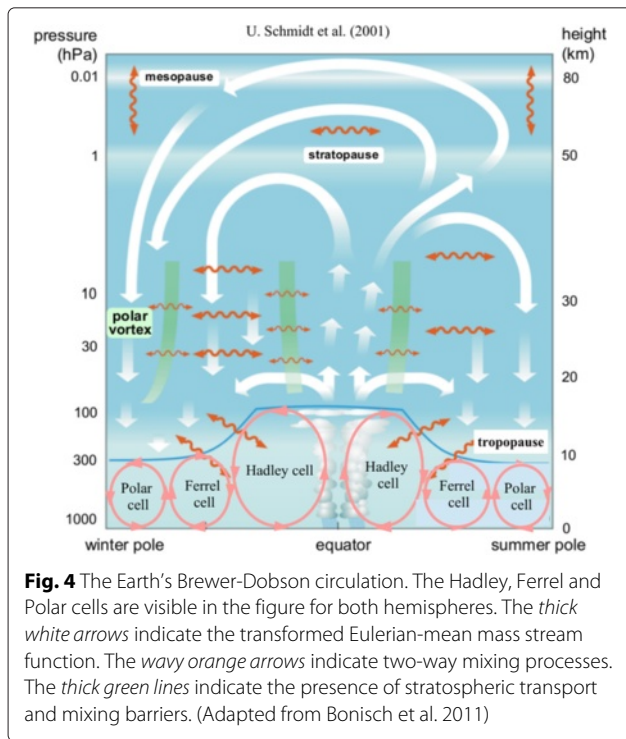
deviations (σ_{PDE}) compared to the CTLE and WTLE standard deviations (σ_{CTLE} and σ_{WTLE} , respectively).

Atmospheric circulation

The tidal lock results in a breakdown of the Brewer-Dobson circulation (Fig. 4) in both the CTLE and the WTLE. As can be seen in Figs. 5, 6, 7, 8 and 9, it is replaced by a very different atmospheric circulation. Despite the atmospheric changes in the circulation, tro-

Table 1 Comparison of the PDE, CTLE and WTLE TOC and the middle stratospheric HW, Ω and T e-folding times, steady-state mean values and their standard deviations

	PDE	σ_{PDE}	CTLE	σ_{CTLE}	WTLE	σ_{WTLE}
TOC (DU)	280.1	1.44	248.7	1.00	248.64	1.42
HW (m/s)	21.19	5.21	14.21	1.00	16.10	2.22
Ω (Pa/s)	-8.6×10^{-7}	9.6×10^{-7}	-1.7×10^{-7}	1.3×10^{-7}	-2.0×10^{-7}	-9.7×10^{-8}
T_{strat} (K)	239.9	0.85	238.4	0.43	239.6	0.27



posphere, stratosphere, and mesosphere are present in both simulations. Below, we present a description of the atmospheric circulation of the two simulations.

Vertical wind

Snapshots of the last model step of the PDE, CTLE, and WTLE vertical wind are shown in Figs. 5, 6 and 7, respectively. The PDE vertical circulation is characterised by

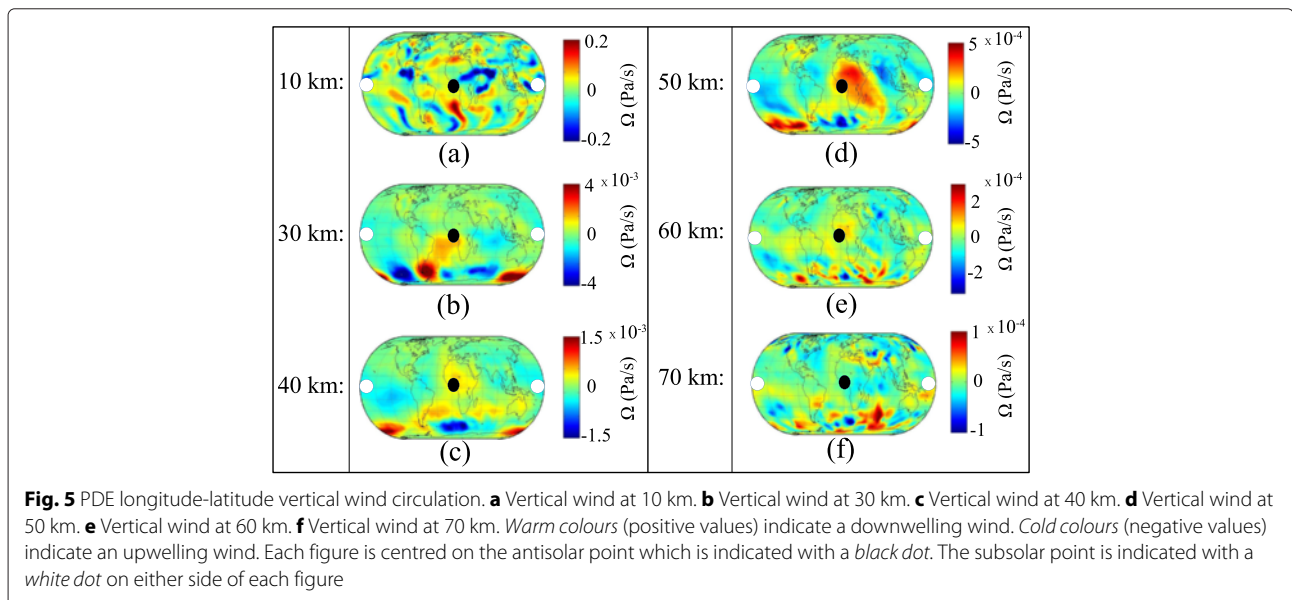
many upwelling and downwelling regions in both the daytime and the nighttime hemispheres. In the tidally locked planets on the other hand, the dayside air rises as a result of being radiatively heated by the constant short-wave radiation flux it receives from the parent star. On the nightside, the lack of incoming radiation results in the radiatively cooling of the air which subsequently sinks towards the surface. This results in the appearance of a dayside upwelling and a nightside downwelling extending from the surface to the mesosphere. Merlis and Schneider (2010) also predicted the presence of such a vertical wind setup for the troposphere of a tidally locked Earth-like aquaplanet orbiting a Sun-like star.

A comparison between Figs. 6 and 7 reveals that the vertical winds of the two simulations are very similar. They are characterised by different small-scale variability vortices and jets of different magnitudes and locations in the CTLE and WTLE simulations. The WTLE atmosphere is characterised by a greater small-scale variability compared to the CTLE. We can, therefore, conclude that the SST change has only a limited effect on the vertical wind.

Horizontal wind

Snapshots of the last model step of the CTLE and WTLE horizontal wind at stratospheric and mesospheric altitudes are shown in Figs. 8 and 9. The CTLE horizontal wind at 24 km is shown in Fig. 8a, while the WTLE horizontal wind at 24 km is shown in Fig. 9a. A comparison between the two figures reveals that in both simulations, the horizontal wind is characterised by the presence of a global eastward zonal jet stream.

The CTLE and WTLE stratospheric horizontal wind at 36 km is shown in Figs. 8b and 9b. In both simulations,



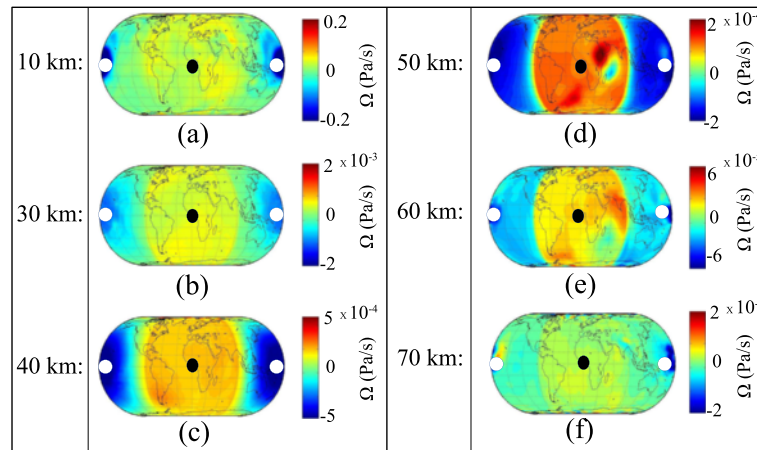


Fig. 6 CTLE longitude-latitude vertical wind circulation. **a** Vertical wind at 10 km. **b** Vertical wind at 30 km. **c** Vertical wind at 40 km. **d** Vertical wind at 50 km. **e** Vertical wind at 60 km. **f** Vertical wind at 70 km. Warm colours (positive values) indicate a downwelling wind. Cold colours (negative values) indicate an upwelling wind. Each figure is centred on the antisolar point which is indicated with a black dot. The subsolar point is indicated with a white dot on either side of each figure

a westward global zonal jet stream with an accompanying vortex located at polar latitudes is present. The vortex can be seen on the left hand side of the Southern and Northern Hemispheres in Figs. 8b and 9b. The blue coloured regions on the right hand side of the Southern and Northern hemispheres, on the other hand, are regions of low HW speeds. The WTLE horizontal wind is slightly weaker and has a wider jet stream compared to the CTLE.

The situation is different at mesospheric altitudes. At 60 km altitude, the zonal jet stream is replaced by large-scale vortices in both the CTLE and the WTLE, located at different geographical locations.

The mesospheric wave-breaking mechanism may explain this phenomenon. Gravity waves are generated by tropospheric convection followed by the release of latent heat. They then propagate upwards and break when they reach the mesosphere. There, they deposit their energy and, in the process, decelerate the wind flow (Nappo 2013). As a result of the different SST heat distributions in the WTLE and CTLE, the convectively induced gravity waves are generated at different locations with different energy budgets. This leads to different wave-breaking patterns and different gravity wave energy dissipation rates and gives rise to different horizontal wind circulation patterns in the two simulations.

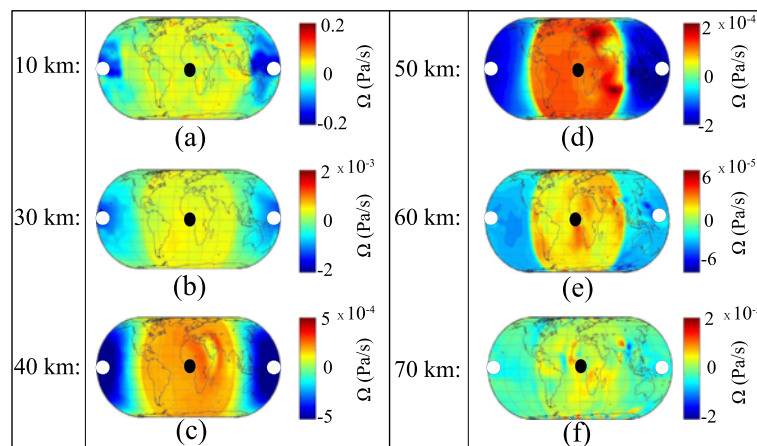


Fig. 7 WTLE longitude-latitude vertical wind circulation. **a** Vertical wind at 10 km. **b** Vertical wind at 30 km. **c** Vertical wind at 40 km. **d** Vertical wind at 50 km. **e** Vertical wind at 60 km. **f** Vertical wind at 70 km. Warm colours (positive values) indicate a downwelling wind. Cold colours (negative values) indicate an upwelling wind. Each figure is centred on the antisolar point which is indicated with a black dot. The subsolar point is indicated with a white dot on either side of each figure

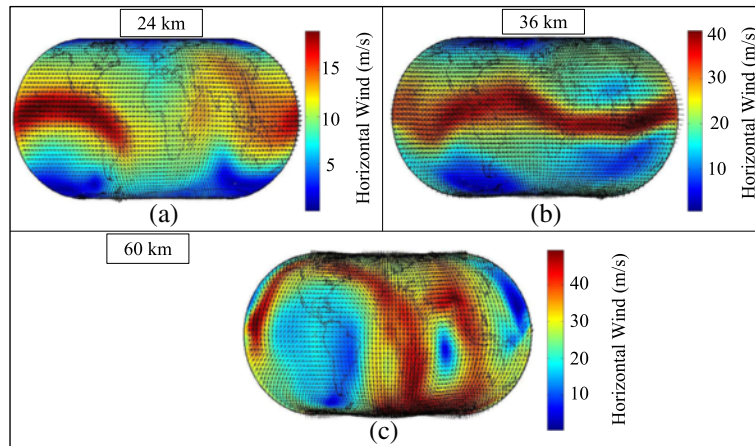


Fig. 8 CTLE horizontal circulation at select altitudes. **a** Horizontal wind at 24 km. **b** Horizontal wind at 36 km. **c** Horizontal wind at 60 km. The black arrows indicate the wind vector while the colour shading shows the wind speed

Gravity waves are also generated through interaction between the planet’s surface orography and the lower tropospheric wind field (Nappo 2013). The encounter between the tropospheric wind and a hill, mountain or mountain range vertically displaces the stably stratified wind flow upwards. This leads to the generation of upwards propagating gravity waves which transport energy and mean-flow momentum towards the middle and upper atmosphere. There, it is deposited through the wave-breaking mechanism (Nappo 2013). In the case of the WTLE and CTLE, both simulations have the same Earth-like orography but different SSTs. As a result different sea and land breezes are generated, which lead to different lower tropospheric horizontal wind distributions (1.4 m/s in average) and therefore different terrain-generated gravity wave distributions. Consequently, the mesospheric energy deposition and wind deceleration are

different for the two simulations. Therefore, the reported changes in the mesospheric horizontal wind are possibly induced by differences in the energy and momentum fluxes of the convectively and orographically generated gravity waves of the two simulations.

As can be seen in Fig. 3b, the middle atmospheric horizontal wind speeds of the CTLE and the WTLE are slower compared to the PDE. They are also characterised by stronger and wider jet streams and the presence of large scale vortices at various geographical locations. The slower wind speeds could be attributed to the smaller CTLE and WTLE Coriolis force, compared to the PDE.

We can, consequently, conclude that the mesospheric circulation is more sensitive to the underlying SST compared to the stratospheric circulation, as is made evident by the regional differences in the vertical and horizontal wind maps. The discrepancy between the stratospheric

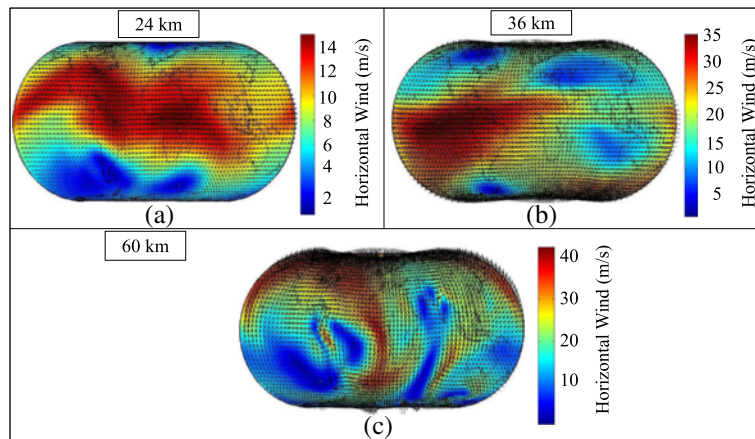


Fig. 9 WTLE horizontal circulation at select altitudes. **a** Horizontal wind at 24 km. **b** Horizontal wind at 36 km. **c** Horizontal wind at 60 km. The black arrows indicate the wind vector while the colour shading shows the wind speed

and mesospheric circulation can be explained by the fact that the stratospheric dynamics are mainly driven by the insolation of stratospheric ozone.

Atmospheric temperature structure

Next, we present the temperature structure of the CTLE and WTLE atmospheres, which can be seen in Fig. 10a. An inspection of Fig. 10a, b, which depicts the snapshots of the last model step, shows that the WTLE’s lower troposphere ($z < 3$ km) is warmer than its CTLE equivalent by a factor of 3.7 K on average. This temperature is generated by the increased upwelling longwave radiation and sensible and latent heat from the underlying WTLE SST which is warmer by approximately 23.7 K compared to the CTLE.

In the 10–15 km region, the WTLE temperature is cooler by 4 K on average compared to the CTLE, as can be seen in the purple highlighted region of Fig. 10b. The adiabatic cooling is generated by the increased upwelling of the subsolar region air, which is radiatively and convectively heated by the warm WTLE SST. This result is in agreement with the studies performed by Rosenlof and Reid (2008), Breasicke and Pyle (2004), Decher and Dameris (2008), who reported the generation of an upper tropospheric cooling by an SST warming, due to the increased deep tropospheric convection generated by the SST warming.

Between 18 and 30 km, the increased upwelling longwave radiation emitted from the warm WTLE SST is absorbed by ozone and radiatively heats the WTLE stratosphere, increasing its temperature by 3.8 on average. This warming is shown in the green highlighted region of Fig. 10b and is in agreement with expectations of radiative coupling between the surface infrared emission and the lower stratosphere.

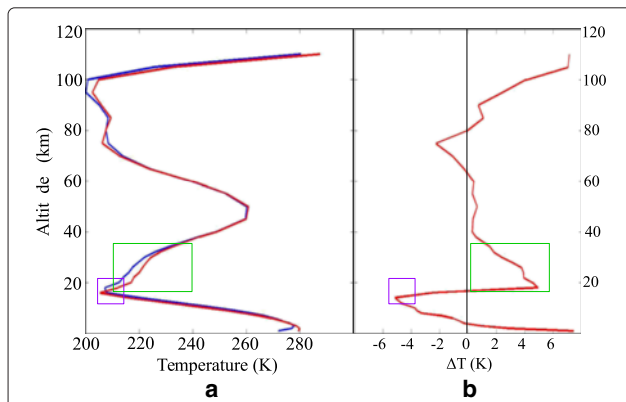


Fig. 10 CTLE and WTLE temperature global mean on day 90. **a** Comparison between the temperature global means of the two planets. The CTLE temperature is depicted using the blue colour line. The WTLE is depicted using the red colour line. The altitude range is 0–120 km. **b** The difference $\Delta T_{altitude}$ of the two planets

To investigate this coupling, we correlate the atmospheric temperature differences with the SST differences obtained from the two simulations. They are calculated by the following equations:

$$\Delta T_{altitude} = T_{WTLE} - T_{CTLE} \tag{2}$$

gives the difference between the WTLE and the CTLE temperatures at a given altitude and geographic location, while

$$\Delta SST = SST_{WTLE} - SST_{CTLE} \tag{3}$$

gives the difference between the WTLE and the CTLE SSTs at a given geographic location.

Figure 11 shows the relationship between the ΔSST and the ΔT at 1 km altitude (ΔT_{1km}). The figure indicates that there is a linear correlation between the two quantities and that the SST changes have a direct radiative effect on the lower tropospheric temperature. Using the least squares method, we determine that the correlation between the ΔSST and the ΔT_{1km} is given by:

$$\Delta T_{24km}(\Delta SST) = (0.2768 \pm 0.0131)\Delta SST + (1.678 \pm 0.394) \tag{4}$$

A 30 K change of the SST corresponds to a 8.3 K change of the lower stratospheric temperature.

Figure 12 shows the relationship between the ΔSST and the ΔT at 24 km altitude (ΔT_{24km}). As can be seen, a linear correlation exists between the ΔSST and ΔT_{24km} , which suggests that SST changes have a direct radiative effect on the lower stratospheric temperature. Using the least square method, we determine that the correlation between the ΔT_{1km} and the ΔT_{24km} is given by

$$\Delta T_{24km}(\Delta SST) = (0.00168 \pm 0.000495)\Delta SST + (3.82 \pm 0.015) \tag{5}$$

A 30 K change of the SST corresponds to a 0.05 K change of the lower stratospheric temperature. The inclination of the regression line is rather small. This may be due to the strong mixing and quasi-isothermal behaviour of the lower stratosphere of tidally locked Earth-like planets.

The above results suggest that the increased thermal radiation emitted by the WTLE’s surface together with the upwelling sensible and latent heat are absorbed by the lower tropospheric greenhouse gases and then increases the WTLE’s temperature. The longwave radiation not absorbed by the lower troposphere reaches the lower stratosphere. There, it is absorbed by the ozone 9.6 μm absorption band, a band expected to be present in the spectra of exoplanets capable of sustaining an ozone layer. Therefore, a stronger absorption line could be expected for warmer SSTs.

The lower mesospheric temperature (70–80 km) on the other hand is cooler by 1.13 K on average compared to

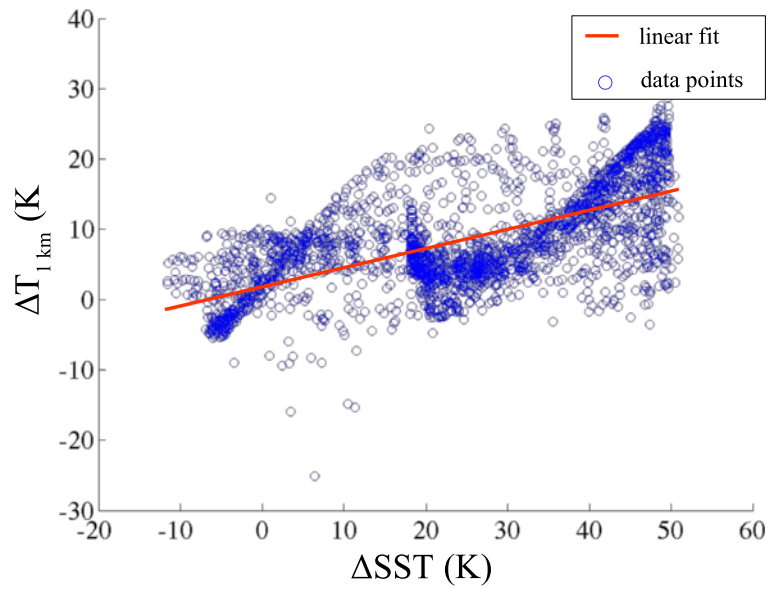


Fig. 11 Scatter plot of ΔSST and ΔT_{1km} . The plot shows the correlation between the surface ΔSST and the ΔT at 1 km altitude, together with a linear regression to the data

the CTLE. This temperature difference can be explained using the mesospheric wave-breaking mechanism mentioned above. The higher number and more energetic gravity waves generated by the warm WTLE SST lead to higher wave momentum deposition in the lower mesosphere and, therefore, to a lower mesospheric adiabatic cooling.

The picture reverses in the upper mesosphere (90–110 km), where the WTLE temperature is higher by 4.3 K on average, compared to the CTLE. This temperature difference may be induced by circulation changes generated by different gravity wave fluxes from below, but the details of the underlying processes remain an open question.

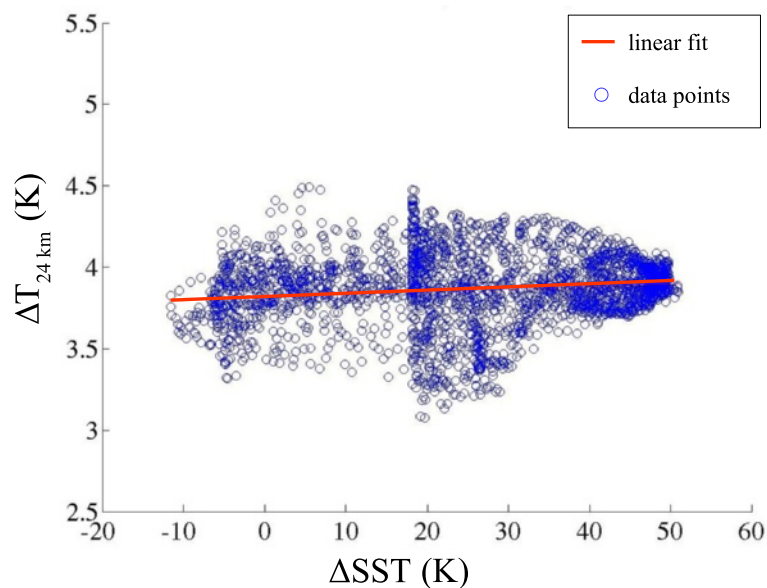


Fig. 12 Scatter plot of ΔSST and ΔT_{24km} . The plot shows the correlation between the surface ΔSST and the ΔT at 24 km altitude, together with a linear regression to the data

We can therefore conclude that increased SST leads to enhanced temperatures in the lower stratosphere of a tidally locked Earth-like exoplanet. Our results indicate that this lower stratospheric heating could be due to the enhanced upwelling of infrared radiation from the warm SST. Generally, the difference between the WLTE and the CLTE simulation is smaller than we expected.

Ozone volume mixing ratio distribution

Figure 13 shows the snapshots of the last model step of the CTLE and WTLE dayside and nightside ozone volume mixing ratio O_3 VMR distribution. It depicts the cross section of the CTLE and WTLE O_3 VMR distribution along the 1st and the 180th meridian, respectively.

A comparison between Figs. 13b and d reveals that the primary ozone layer (30–40 km altitude) is not significantly affected. The increased WTLE middle atmospheric temperature (Fig. 10) results in the decrease of the WTLE dayside O_3 VMR by 1.8 % and a nightside decrease of 1.27 %.

On the other hand, the nighttime secondary ozone layer, located in both cases in the 85–110 km altitude range, is significantly affected. On Earth, the secondary ozone layer appears only during nighttime. On the daytime hemisphere, the strong UV radiation destroys any ozone molecules that might form shortly after their creation. On the nightside, ozone is generated and accumulated on the nightside by recombination of atomic and molecular oxygen.

The WTLE O_3 VMR is enhanced by 40.5 % compared to the CTLE. It is possible that the mesospheric circulation changes, generated by the different upwelling gravity wave fluxes, are responsible for the changes in the secondary ozone layer, but the details of the underlying processes remain an open question.

We can, therefore, conclude that the use of an inaccurate SST in a tidally locked Earth-like exoplanet may significantly affect the secondary ozone layer, while the primary ozone layer remains almost unaffected.

The gap visible at mesospheric altitudes over the WTLE equator in Fig. 13a appears as a result of local upwelling of ozone-poor air from lower altitudes and is located in the regions close to the Atlas mountains and the Atlantic Ocean. It is possibly generated by upwelling gravity waves, not present in the CTLE.

Conclusions

We studied the sensitivity of a tidally locked Earth-like atmosphere to its underlying SST by simulating the atmospheric circulation, temperature, and ozone distribution changes generated by two different SST distributions. The first SST distribution represented the well-observed SST of the fast-rotating, present-day Earth, and the simulation using it was named WLTE. The second SST distribution was the SST of a tidally locked Earth-like aquaplanet. It was provided by Merlin and Schneider (2010) and the simulation using it was named CLTE.

The main conclusion of our study is that for slow-rotating planets, the drastic SST changes do not lead to similarly strong changes in the middle atmosphere of the planet, as the vertical and horizontal winds, the primary ozone layer and the atmospheric thermal structure are relatively insensitive to the changes in the underlying SST.

The underlying SST changes result in small-scale variability changes of the vertical and horizontal winds. The strongest effect appears at mesospheric altitudes, possibly due to differences in the upwelling gravity wave flux generated by the different SST distributions. Our results are of interest for both exoplanets and for Earth climate trend studies.

The primary ozone layer O_3 VMR is altered by 1.8 % on the dayside and by 1.27 % on the nightside. The secondary ozone layer, on the other hand, is altered by 40.5 %. The

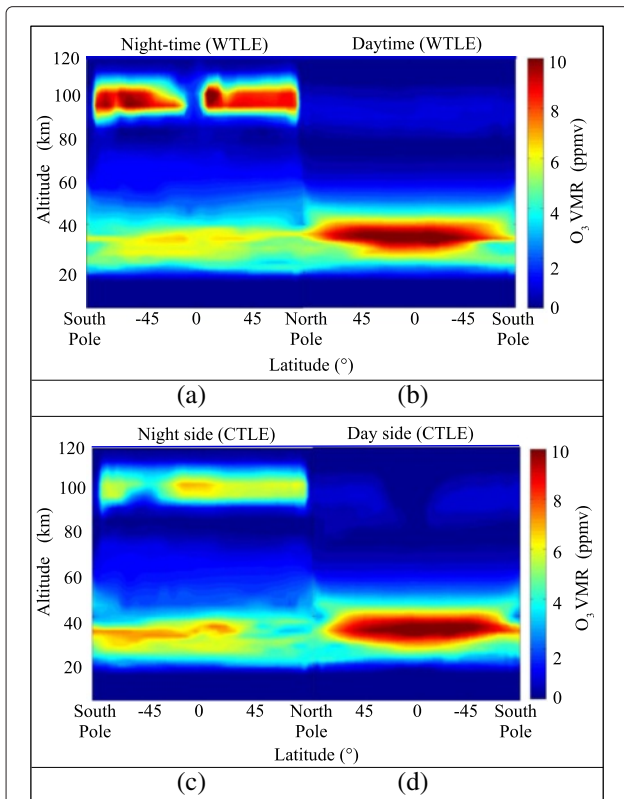


Fig. 13 WTLE and CTLE height-latitude cross section of O_3 VMR along the meridian through the subsolar point and the antisolar point. **a** Vertical cross section of the WTLE nighttime hemisphere. **b** Vertical cross section of the WTLE daytime hemisphere. **c** Vertical cross section of the CTLE nightside hemisphere. **d** Vertical cross section of the CTLE dayside hemisphere

generation mechanism is currently an open question and under investigation.

The lower tropospheric temperature global average is increased, on average, by 3.7 K compared to the CTLE due to the warmer WTLE SST. The WTLE tropospheric warming causes the hot air to ascend and cool adiabatically, generating a cooling of 4 K on average in the altitude regions between 10 and 15 km, compared to the CTLE. This result is in agreement with past studies on the effects of SST warmings on the Earth's upper troposphere. Between 18 and 30 km, a stratospheric heating of 3.8 K on average, is present in the WTLE compared to the CTLE, generated by the absorption of the upwelling longwave radiation by ozone through the 9.6 μm line. The enhanced, upwelling longwave radiation is generated by the warmer WTLE SST. The lower mesospheric cooling (1.13 K) on average is also generated by the warmer WTLE, due to increased wave generation and subsequent wave-breaking in the mesosphere. An upper mesospheric warming (4.3 K) is also present in the WTLE compared to the CTLE, but its generation mechanism is currently an open question and under investigation.

Our results show that the majority of the changes in the middle atmospheric circulation appear due to the tidal locking which results in the breakdown of the Brewer-Dobson circulation. The vertical circulation is replaced by a dayside downwelling, centred on the subsolar point and a nightside upwelling, centred on the antisolar point. The tidal locking also alters the horizontal wind at all altitudes, resulting in lower wind speeds, wider and stronger jet streams and the appearance of large scale vortices at various locations compared to the PDE, possibly due to the reduced Coriolis force of the TLE.

A future study would aim to explain the physical processes responsible for the increase of the upper mesospheric temperature and strengthening of the secondary ozone layer accompanying the increase in the underlying SST.

Abbreviations

ATM, atmospheric geophysical model; CESM, community earth system model; CICE, sea-ice data model; CLM, community land model; CPL, coupler of the CESM; docn, prescribed data ocean model; GLC, land-ice geophysical model; ICE, sea-ice geophysical model; LND, land geophysical model; MODIS, moderate-resolution imaging spectroradiometer; NOAA, National oceanic and atmospheric administration; OCN, ocean geophysical model; SZA, solar zenith angle; TLE, tidally locked earth; WTLE, warm tidally locked earth; CTLE, cold tidally locked earth; TOC, total O₃ Content; WACCM, whole atmosphere community climate model; HW, horizontal wind; Ω , vertical wind; E_{kin} , integrated atmospheric kinetic energy; T, temperature; O₃VMR, ozone volume mixing ratio

Acknowledgements

We would like to thank the Center for Space and Habitability (University of Bern) for the PhD fellowship and the Institute of applied Sciences (University of Bern) for the funding that made this study possible. We would like to thank the WACCM forum for the invaluable information it provided. We would also like to thank Ansgar Schanz and Martin Leiner for the computer technical

support they provided. Finally, we would like to thank Niklaus Kämpfer and Helmut Lammer for the valuable discussions and advises.

Authors' contributions

EP performed the simulations and the data analysis. KH contributed to the data analysis and the interpretation. PW contributed to the revising of the paper. All authors read and approved the final manuscript.

Competing interests

The authors declare that they have no competing interests.

Author details

¹Institute of Applied Physics, University of Bern, Sidlerstrasse 5, 3012 Bern, Switzerland. ²Center for Space and Habitability, University of Bern, Sidlerstrasse 5, 3012 Bern, Switzerland. ³Oeschger Centre for Climate Change Research, University of Bern, Falkenplatz 16, 3012 Bern, Switzerland. ⁴Physics Institute, University of Bern, Sidlerstrasse 5, 3012 Bern, Switzerland.

Received: 22 January 2016 Accepted: 4 July 2016

Published online: 29 July 2016

References

- Braesicke P, Pyle JA (2004) Sensitivity of dynamics and ozone to different representations of SSTs in the unified model. *Q J R Meteorol Soc* 130:2033–2045. doi:10.1256/qj.03.183
- Chen G, Plumb RA, Lu J (2010) Sensitivities of zonal mean atmospheric circulation to SST warming in an aquaplanet model. *Geophys Res Lett* 37:12701. doi:10.1029/2010GL043473
- Clough S, Iacono M (1995) Line-by-line calculation of atmospheric fluxes and cooling rates 2. Application to carbon dioxide, ozone, methane, nitrous oxide and the halocarbons. *J Geophys Res* 100:16519–16535. doi:10.1029/95JD01386
- Clough SA, Shephard MW, Mlawer EH, Delamere JS, Iacono MJ, Cady-Pereira K, Boukabara S, Brown PD (2005) Atmospheric radiative transfer modeling: a summary of the AER codes. *J Quant Spectrosc Radiat Transfer* 91:233–244. doi:10.1016/j.jqsrt.2004.05.058
- Davis RN, Du J, Smith AK, Ward WE, Mitchell NJ (2013) The diurnal and semidiurnal tides over Ascension Island (9° S, 14° W) and their interaction with the stratospheric quasi-biennial oscillation: studies with meteor radar, eCMAM and WACCM. *Atmos Chem Phys* 13(18):9543–9564
- Deckert R, Dameris M (2008) Higher tropical SSTs strengthen the tropical upwelling via deep convection. *Geophys Res Lett* 35:10813. doi:10.1029/2008GL033719
- Godolt M, Grenfell JL, Hamann-Reinus A, Kitzmann D, Kunze M, Langematz U, von Paris P, Patzer ABC, Rauer H, Stracke B (2015) 3D climate modeling of Earth-like extrasolar planets orbiting different types of host stars. *Planetary Space Sci* 111:62–76. doi:10.1016/j.pss.2015.03.01
- Grenfell JL, Stracke B, von Paris P, Patzer B, Titz R, Segura A, Rauer H (2007) The response of atmospheric chemistry on earthlike planets around F, G and K Stars to small variations in orbital distance. *Planetary Space Sci* 55:661–671. doi:10.1016/j.pss.2006.09.00
- Grenfell JL, Gebauer S, Godolt M, Palczynski K, Rauer H, Stock J, von Paris P, Lehmann R, Selsis F (2013) Potential biosignatures in super-earth atmospheres II. Photochemical responses. *Astrobiology* 13:415–438. doi:10.1089/ast.2012.0926
- Grenfell JL, Gebauer S, Paris P, v, Godolt M, Rauer H (2014) Sensitivity of biosignatures on Earth-like planets orbiting in the habitable zone of cool M-dwarf stars to varying stellar UV radiation and surface biomass emissions. *Planetary Space Sci* 98:66–76. doi:10.1016/j.pss.2013.10.00
- Haberle RM, McKay CP, Tyler D, Reynolds RT, Doyle LR (1996) Circumstellar Habitable Zones. In: Doyle LR (ed). *Proceedings of The First International Conference*. Travis House Publications, Menlo Park, CA, p 29
- Hegyi BM, Deng Y, Black RX, Zhou R (2014) Initial transient response of the winter polar stratospheric vortex to idealized equatorial pacific sea surface temperature anomalies in the ncar waccm. *J Clim* 27:2699–2713. doi:10.1175/JCLI-D-13-00289.1
- Iacono M, Delamere J, Mlawer M, Shephard E, Clough S, Collins W (2008) Radiative forcing by long-lived greenhouse gases: calculations with the AER radiative transfer models. *J Geophys Res Atmos*:113. doi:10.1029/2008JD009944

- Joshi MM, Haberle RM, Reynolds RT (1997) Simulations of the atmospheres of synchronously rotating terrestrial planets orbiting M dwarfs Conditions for atmospheric collapse and the implications for habitability. *Icarus* 129:450–465
- Joshi M (2003) Climate model studies of synchronously rotating planets. *Astrobiology* 3(2):415–427. doi:10.1089/15311070376901648
- Lean J (2000) Evolution of the sun's spectral irradiance since the maunder minimum. *Geophys Res Lett* 27(16):2425–2428. doi:10.1029/2000GL000043
- Liu X, Liu H-L, Liu AZ, Yue J, McInerney JM, Li Z (2012) Momentum budget of the migrating diurnal tide in the Whole Atmosphere Community Climate Model at vernal equinox. *J Geophys Res Atmos*:17. http://dx.doi.org/10.1002/2013JA019421
- Merlis TM, Schneider T (2010) Atmospheric dynamics of Earth-like tidally locked aquaplanets. *J Adv Model Earth Syst* 2:13. doi:10.3894/JAMES.2010.2.1
- Mlawer E, Taubman S, Brown P, Iacono M, Clough S (1997) Radiative transfer for inhomogeneous atmospheres: RRTM, a validated correlated-k model for the longwave. *J Geophys Res* 102:16663–16682. doi:10.1029/97JD00237
- Nappo CJ (2013) An introduction to atmospheric gravity waves. Academic Press
- National Oceanic and Atmospheric Administration's Space Environment Center (2016). wikipedia: http://www.swpc.noaa.gov/
- Neale RB, Gettelman A, Park S, Chen C, Lauritzen PH, Williamson DK, Conley AJ, Kinnison D, Marsh D, Smith AK, Vitt F, Garcia R, Lamarque JF, Mills M, Tilmes S, Morrison H, Cameron-Smith W, Collins WD, Iacono MT, Easter RC, Liu X, Ghan SJ, Rasch PJ, Taylor MA (2012) Description of the NCAR Community Atmosphere Model (CAM 5.0). CESM database. http://www.cesm.ucar.edu/models/cesm1.0/cam/docs/description/cam5_desc.pdf
- Pedatella NM, Liu H-L (2013) Influence of the El Niño Southern Oscillation on the middle and upper atmosphere. *J Geophys Res Space Phys* 118:2744–2755. http://dx.doi.org/10.1002/2013JA019421
- Pedatella NM, Fuller-Rowell T, Wang H, Jin H, Miyoshi Y, Fujiwara H, Shinagawa H, Liu H-L, Sassi F, Schmidt H, Matthias V, Goncharenko L (2014) The neutral dynamics during the 2009 sudden stratosphere warming simulated by different whole atmosphere models. *J Geophys Res Space Phys*. http://dx.doi.org/10.1002/2013JA019421
- Proedrou E, Hocke K (2016) Characterising the three-dimensional ozone distribution of a tidally locked earth-like planet. *Earth Planets Space* 68(1):1–20. doi:10.1186/s40623-016-0461-x
- Rauer H, Gebauer S, Paris PV, Cabrera J, Godolt M, Grenfell JL, Belu A, Selsis F, Hedelt P, Schreier F (2011) Potential biosignatures in super-Earth atmospheres I. Spectral appearance of super-Earths around M dwarfs. *Astron Astrophys* 529:8. doi:10.1051/0004-6361/20101436
- Rosenlof KH, Reid GC (2008) Trends in the temperature and water vapor content of the tropical lower stratosphere: sea surface connection. *J Geophys Res* 113:06107. doi:10.1029/2007JD009109
- Rugheimer S, Kaltenegger L, Zsom A, Segura A, Sasselov D (2013) Spectral fingerprints of Earth-like planets around FGK stars. *Astrobiology* 13:251–269. doi:10.1089/ast.2012.088
- Sander SP, Friedl RR, Ravishankara AR, Golden DM, Kolb CE, Kurylo MJ, Molina MJ, Moortgat GK, Keller-Rudek H, Finlayson-Pitts BJ, Wine PH, Huie RE, Orkin VL (2006) Chemical kinetics and photochemical data for use in atmospheric studies. Evaluation Number 15. National Aeronautics and Space Administration, Jet Propulsion Laboratory, Pasadena, CA
- Segura A, Krellove K, Kasting JF, Sommerlatt D, Meadows V, Crisp D, Cohen M, Mlawer E (2003) Ozone concentrations and ultraviolet fluxes on Earth-like planets around other stars. *Astrobiology* 3:689–708. doi:10.1089/15311070332273602
- Segura A, Kasting JF, Meadows V, Cohen M, Scalo J, Crisp D, Butler RAH, Tinetti G (2005) Biosignatures from Earth-like planets around M-dwarfs. *Astrobiology* 5:706–725. doi:10.1089/ast.2005.5.70
- Segura A, Walkowicz LM, Meadows V, Kasting J, Hawley S (2010) The Effect of a strong stellar flare on the atmospheric chemistry of an Earth-like planet orbiting an M Dwarf. *Astrobiology* 10:751–776. doi:10.1089/ast.2009.037
- Selsis F (2000) Darwin and Astronomy the Infrared Space Interferometer. In: Schürmann B (ed). ESA Special Publication, vol 451. p 133
- Smith KL, Polvani LM, Marsh DR (2012) Mitigation of 21st century Antarctic sea ice loss by stratospheric ozone recovery. *Geophys Res Lett* 39(20):L20701. doi:10.1029/2012GL053325, http://dx.doi.org/10.1029/2012GL053325
- Solomon S, Qiang L (2005) Solar extreme-ultraviolet irradiance for general circulation models. *J Geophys Res* 110:10306. doi:10.1029/2005JA011160
- Tan B, Chu X, Liu H-L, Yamashita C, Russell JM (2012a) Atmospheric semidiurnal lunar tide climatology simulated by the whole atmosphere community climate model. *J Geophys Res* 117:1–11. doi:10.1029/2012JA017792
- Tan B, Chu X, Liu H-L, Yamashita C, Russell JM (2012b) Zonal-mean global teleconnection from 15 to 110 km derived from SABER and waccm. *J Geophys Res Atmos* 117:1–11. doi:10.1029/2011JD016750
- Tan B, Chu X, Liu H-L, Yamashita C, Russell JM (2012c) Parameterization of the inertial gravity waves and generation of the quasi-biennial oscillation. *J Geophys Res Atmos*:117. doi:10.1029/2011JD016778
- Tarter JC, Backus PR, Mancinelli RL, Aurnou JM, Backman DE, Basri GS, Boss AP, Clarke A, Deming D, Doyle LR, Feigelson ED, Freund F, Grinspoon DH, Haberle RM, Hauck SAI, Heath MJ, Henry TJ, Hollingsworth JL, Joshi MM, Kilston S, Liu MC, Meikle E, Reid IN, Rothschild LJ, Scalo J, Segura A, Tang CM, Tiedje JM, Turnbull MC, Walkowicz LM, Weber AL, Young RE (2007) A reappraisal of the habitability of planets around M dwarf stars. *Astrobiology* 7:30–65. doi:10.1089/ast.2006.012
- Verstein M, Craig T, Middleton A, Feddema D, Fisher C (2012). CESM 1.0.4 user's guide. available from: http://www.cesm.ucar.edu/models/cesm1.0/cesm/cesm_doc_1_0_4/book1.html
- Wang Y-M, Lean JL, Sheeley NRJ (2005) Modeling the sun's magnetic field and irradiance since 1713. *Astrophys J* 625(1):522
- Wikipedia U.S Standard Atmosphere (2016). https://en.wikipedia.org/wiki/U.S._Standard_Atmosphere
- Yang J, Cowan NB, Abbot DS (2013) Stabilizing cloud feedback dramatically expands the habitable zone of tidally locked planets. *Astrophys J Lett* 771:45. doi:10.1088/2041-8205/771/2/L4

Submit your manuscript to a SpringerOpen® journal and benefit from:

- Convenient online submission
- Rigorous peer review
- Immediate publication on acceptance
- Open access: articles freely available online
- High visibility within the field
- Retaining the copyright to your article

Submit your next manuscript at ► springeropen.com